Hierarchical Triple-Maglev Dual-Rate Control Over a Profibus-DP Network

Ricardo Pizá, Julián Salt, *Member, IEEE*, Antonio Sala, *Member, IEEE*, and Ángel Cuenca, *Member, IEEE*

Abstract—This paper addresses a networked control system application on an unstable triple-magnetic-levitation setup. A hierarchical dual-rate control using a Profibus-decentralized peripherals network has been used to stabilize a triangular platform composed of three maglevs. The difficulty in control is increased by time-varying network-induced delays. To solve this issue, a local decentralized $\mathcal{H}_\infty$ control action is complemented by means of a lower rate output feedback controller on the remote side. Experimental results show good stabilization and reference position accuracy under disturbances.

Index Terms—Dual-rate control systems, linear matrix inequality, maglev, network delay, networked control systems, Profibus, stability analysis.

I. INTRODUCTION

WHEN a control application is projected on a network-based environment, in which different devices (sensor, actuator, controller) are connected by means of a shared communication medium [1]–[3], typical problems such as data packet losses, lack of synchronization among devices, bandwidth limitations, and time-varying delays occur.

In some cases, the controlled process is very sensitive to these problems. That is the case with a maglev-based platform [4], [5] in network-based control [6]. This magnetic levitation process control problem is challenging because each one of the systems that configure the platform are unstable and non-linear. Maglev platforms have also been used to demonstrate applicability of control strategies in research literature [7], [8].

Also, magnetic levitation has a wide range of applications [9], [10]. Thus, this paper demonstrates some network-based hierarchical control techniques in a three-maglev platform.

Regarding the network to be selected in control, there are plenty of options with current technology. In an unstable fast system such as the one under consideration, a low-latency high-bandwidth network would be a reasonable choice, for

example, a network based on traditional field bus protocols such as Profibus, DeviceNet, CAN, InterBus, Field Bus, etc., or a network based on newer industrial Ethernet protocols such as ProfiNET, EtherNet/IP, Powerlink, EtherCAT, Modbus TCP, or SERCOS III [11]. Any of these networks may be suitable for controlling this platform.

In this paper, a Profibus-decentralized peripherals (DP) with asynchronous operation mode has been selected [12]. Some characteristics of Profibus make this network especially interesting and challenging from a control engineering point of view. There are two kinds of delays in this network: one is the delay induced by data transfer between buffers and nodes; and the other one is the delay that appears in the transmission between network nodes, whereby a distribution of time-varying communication delay appears. The chosen control strategy will also require a triggered bus mechanism for synchronization based on Profibus freeze and sync commands. Other Profibus-based control applications are reported in [13] and [14].

The objective of this paper is to experimentally demonstrate a methodology, described below, for designing hierarchical network-based control systems for a multivariable unstable plant when computational capabilities and network bandwidth/sampling rates are restricted and data transfer delays are present.

Therefore, a hierarchical control system is proposed here, as depicted in Fig. 1. Indeed, due to the limitations in sampling rate and the communication delay magnitudes, it was not possible to design a single stabilizing remote control in the maglev platform. Consequently, first of all, a fast-rate local decentralized controller is designed and, in the following step, a more sophisticated slower rate "coordinating" remote control is designed. Because of the lack of shared information, the decentralized controllers (which work perfectly with one maglev) performed badly with the three-maglev platform in place, falling frequently: neither the local-only nor the remote-only solutions were satisfactory.

For each maglev, a standalone local controller has been designed and implemented using robust $\mathcal{H}_\infty$ control techniques [15]. The remote controllers have been designed using linear matrix inequality (LMI) gridding techniques [16].

The rest of this paper is organized as follows. Section II describes the physical process (the triple-maglev system) used as a test platform in the experiments. Section III (and an additional appendix) presents how this process is modeled and linearized. The hierarchical control structure is introduced in Section IV. Before presenting the experimental results in Section VI, some network and hardware configuration aspects

Fig. 1. Hierarchical control structure.

Fig. 2. Experimental setup.

Fig. 3. Illustrations of the experimental setup.
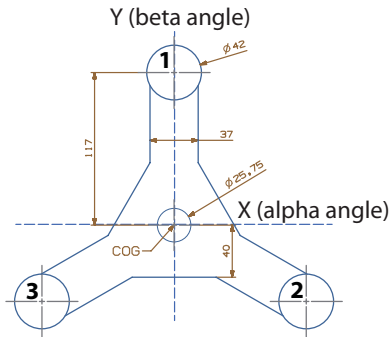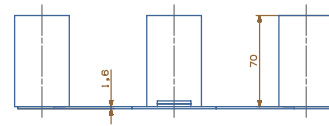
Fig. 4. Platform dimensions (top and side view), reference model axis, and maglev numeration.
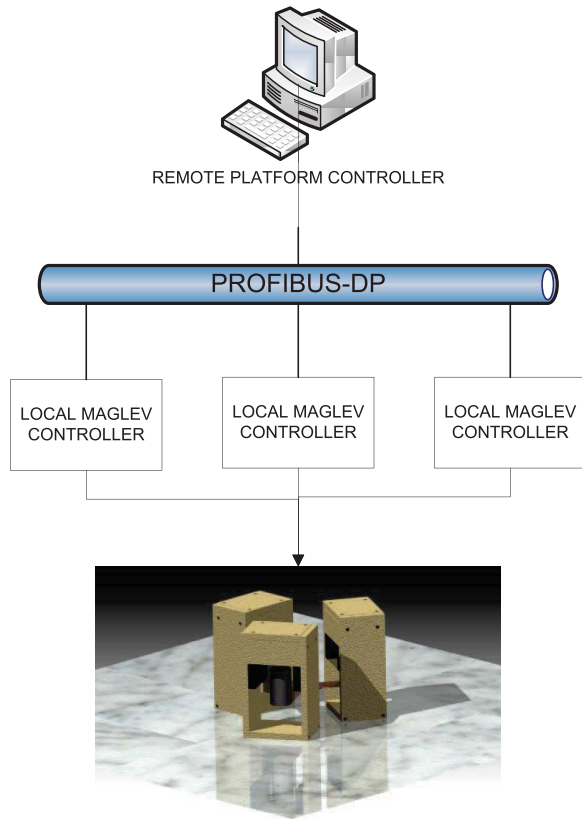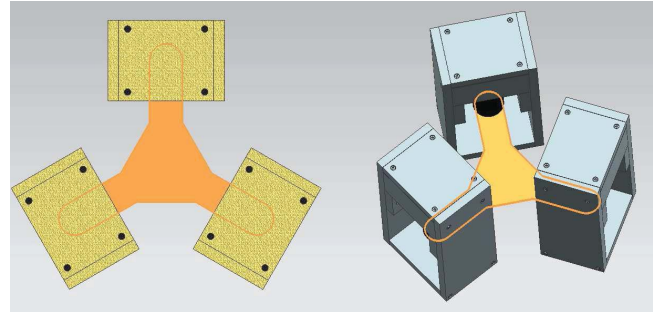
used in these experiments are detailed in Section V. Finally, Section VII concludes this paper.

II. THREE-MAGLEV PLATFORM DESCRIPTION

The experimental platform used in this paper comprises several elements:

1) three magnetic levitation units. These units can be operated in a standalone way, as done in experiment 1 in later sections;
2) a Y-shaped levitated platform to which individual maglevs can be attached;
3) a National Instruments CompactRio 9074 acting as a local controller;
4) a desktop PC acting as a remote controller;
5) a Profibus-DP network.

Let us now describe the most relevant characteristics of these elements.

The controlled plant is a levitated platform, shown in Fig. 2 (left). This levitated platform has the shape of an equilateral triangle with permanent magnets located at the corners of the platform. A drawing scheme is shown in Fig. 3. The vertical position of each magnet is controlled by an electromagnet. Thus, there are three maglevs located at the terminals of the platform. Each maglev takes a voltage input signal to generate the magnetic field and takes the vertical position measure using a set of infrared sensor arrays.

The levitators have been provided by extra dimension technologies (http://www.xdtech.com), model ML-EA.

The magnetic levitation unit includes its own levitator along with its power amplifier unit. The maglev provides position information, from the infrared sensor array in ±10 V range. The control signal to be provided to the power amplifier must be also in ±10 V range.

In order to build the coupled platform, the three independent loads of the maglevs were attached to the above-referred Y-shaped aluminum sheet. Fig. 4 shows a drawing with the levitated structure. The dimensions are in millimeters, and in the center of the platform the circular shapes correspond to an extra load (a 2-euro coin, 8.5 g) used in transient analysis experiments. The total weight for the levitated platform is 0.423 kg.

Further details on the model parameters relevant for control are discussed in the Appendix.

A similar maglev platform can be found in other works, for example, in [17], as well as those based on predictive

control [18], fuzzy control [19], [20], or some nonlinear control methods [21].

III. MODELING AND LINEARIZATION

This section discusses how the specific model is obtained and linearized in order to apply the control scheme proposed in later sections.

A. Single Maglev Modeling

The well-known Lagrange equations [22] can be used to derive the differential equations of electromechanical systems

$$\frac{d}{dt}\frac{\partial T}{\partial \dot{q}} - \frac{\partial T}{\partial q} + \frac{\partial D}{\partial \dot{q}} + \frac{\partial V}{\partial q} = F_G$$

where T, V, and D represent the generalized kinetic,[1] potential, and dissipation energies, respectively. F_G denotes the generalized forces, and the variable q express one of the generalized coordinates.

Let us denote the air gap between the variable magnet and the levitated load with the variable z. Assuming infinite permeability except at the air gap with permeability μ, and uniform magnetic flux density B, the energy T_{mag} stored in the levitator's air gap is

$$T_{\mathrm{mag}} = \frac{B^2}{2\mu} \cdot A \cdot z$$

where A is the cross-sectional area and B given by $F_\mu \mathrm{m}/z$, where F_m stands for the magnetomotive force [linear with current NI (coil) plus a permanent magnet component I_0, N being the number of turns of the inductor]. In summary, the magnetic energy is

$$T_{\mathrm{mag}} = \frac{(NI + I_0)^2 \mu A}{2z}. \tag{1}$$

The reader is referred to [23] (for instance) for details on magnetic field modeling.

Adding the mechanical kinetic energy term $T_{\mathrm{mech}} = 1/2m\dot{z}^2$, the gravitational potential $V = -mgz$, the resistive dissipation $R \cdot i$, and using both charge and air gap as generalized coordinates, the following nonlinear model can be obtained (details omitted for brevity, see [24] for similar modeling problems):

$$m\ddot{z} - \frac{\mu(NI + I_0)^2 A}{4z^2} - mg = 0 \tag{2}$$

$$\frac{\mu A N^2}{z}\dot{I} + \frac{\mu A N(I_0 + NI)\dot{z}}{z^2} + RI = V. \tag{3}$$

Of course, the uniform-magnetic-field model is not exact, as there exist lateral and bottom air gaps. In addition, if the intensity polarity were abruptly changed, the flux lines for the resulting magnetic field would be modified; however, we assume that such situations will not occur around the chosen operation point.

---

[1]To avoid confusion, note that T will later denote sampling rate, but symbolizing in this way kinetic energy keeps notation in this section similar to standard mechanics textbooks.

Equations (2) and (3), define the theoretical model. Assuming a suitable operating point, a linearized single maglev continuous-time model is obtained as

$$\frac{M}{3} \cdot \ddot{z}(t) = f(t) \tag{4}$$

$$f(t) = K_1 I(t) + K_2 \cdot z(t) \tag{5}$$

$$L\dot{I}(t) + Q \cdot \dot{z}(t) + RI(t) = v(t) \tag{6}$$

where $M/3$ is the mass of the whole levitated platform corresponding to one levitator, f is the electromagnetic force, and the constants L, R, K_1, and K_2 are available in the levitator's manual provided by the manufacturer. The parameter Q models the potential induced by the movement of the levitated magnet.[2] The maglev's numerical values for the parameters can be found in Appendix.

Introducing a measurement equation

$$y(t) = K_3 \cdot z(t) \tag{7}$$

the variable y is the position measurement taken with the infrared sensor system, with K_3 a linearized calibration constant available on the maglev user's manual.

These equations can be expressed in state space form for a generic maglev i as

$$\begin{pmatrix} \dot{I}_i(t) \\ \dot{z}_i(t) \\ \ddot{z}_i(t) \end{pmatrix} = \begin{pmatrix} \frac{-R_i}{L_i} & 0 & \frac{-Q^i}{L_i} \\ 0 & 0 & 1 \\ \frac{3K_1^i}{M} & \frac{3K_2^i}{M} & 0 \end{pmatrix} \cdot \begin{pmatrix} I_i(t) \\ z_i(t) \\ \dot{z}_i(t) \end{pmatrix} + \begin{pmatrix} \frac{1}{L_i} \\ 0 \\ 0 \end{pmatrix} \cdot v_i(t)$$

$$y_i(t) = \begin{pmatrix} 0 & K_3^i & 0 \end{pmatrix} \cdot \begin{pmatrix} I_i(t) \\ z_i(t) \\ \dot{z}_i(t) \end{pmatrix}. \tag{8}$$

B. Global Platform (Coupled) Model

When the global three-levitator platform is considered, its position will be determined by the height of the center of mass and by two angular coordinates.[3] Rigid-body dynamic equations must be then considered.

First of all, the meaning of z will be changed to denote the vertical displacement of the platform's center of mass (z_i will denote each maglev's). The linear motion is only considered along the z-axis

$$M\ddot{z} = \sum_i f_i.$$

Second, denoting the resulting torque vector as τ, the rotation of the platform around the center of gravity yields

$$J\dot{\omega} = \tau - \omega \times (J\omega)$$

---

[2]It has been estimated in a separate experiment by moving the maglev and measuring position and induced voltage (opening the circuit). A least squares fit between a filtered numerical derivative of the position and the voltage has been used (details omitted for brevity).

[3]The rest of the degrees of freedom, i.e., rotation around the vertical axis and two horizontal displacement coordinates, cannot be controlled with the available actuators. Fortunately, as the levitators are somehow attracted toward the electromagnets also in the horizontal axis, these uncontrollable models are stable. Nevertheless they are only very lightly damped (by air, eddy currents, etc.; actually, damping is so subtle that it has not been considered in the controlled–vertical coordinate movement): the platform must be carefully and slowly positioned without introducing significant energy on these coordinates.

where J is the inertia matrix. However, when linearizing around zero rotational speed, and choosing small rotations around the principal axis (diagonal inertia matrix) as angular coordinates, then the following equalities can be considered, α and β being the angles of rotation of levitated platform around X and Y axes, respectively:

$$J_{xx}\ddot{\alpha} = \tau_x \qquad (9)$$

$$J_{yy}\ddot{\beta} = \tau_y \qquad (10)$$

τ_x and τ_y being the torques on axis x and y, respectively, with the chosen reference frame as shown in Fig. 4.

Expressions of torques at the center of gravity from each of the maglev electromagnetic forces are as follows:

$$\tau_{1x} = f_1 L \cos \alpha, \quad \tau_{1y} = 0$$
$$\tau_{2x} = f_2 L \cos \alpha \cos \beta \sin \frac{\pi}{6}, \quad \tau_{2y} = f_2 L \cos \alpha \cos \beta \sin \frac{\pi}{3}$$
$$\tau_{3x} = f_3 L \cos \alpha \cos \beta \sin \frac{\pi}{6}, \quad \tau_{3y} = f_3 L \cos \alpha \cos \beta \sin \frac{\pi}{3}$$

where L is the length of the arm, and α and β are the rotation angles around the x- and y-axis, respectively.

For sensor measurements, the expressions are as follows:

$$z_1 = z + L\alpha$$
$$z_2 = z - L \sin \frac{\pi}{6} \cdot \alpha + L \sin \frac{\pi}{3} \cdot \beta$$
$$z_3 = z + L \sin \frac{\pi}{6} \cdot \alpha - L \sin \frac{\pi}{3} \cdot \beta.$$

Then, the equation of movement in the vertical direction is

$$M\ddot{z} = f_1 + f_2 + f_3.$$

The linearized torques around the horizontal position are

$$\tau_{1x} = f_1 L, \quad \tau_{1y} = 0$$
$$\tau_{2x} = f_2 L \sin \frac{\pi}{6}, \quad \tau_{2y} = f_2 L \sin \frac{\pi}{3}$$
$$\tau_{3x} = f_3 L \sin \frac{\pi}{6}, \quad \tau_{3y} = f_3 L \sin \frac{\pi}{3}.$$

Hence, the overall linearized system equations are as follows:

$$L_1 \dot{I}_1 + Q_1 \cdot \dot{z}_1 + R_1 I_1 = v_1$$
$$L_2 \dot{I}_2 + Q_2 \cdot \dot{z}_2 + R_2 I_2 = v_2$$
$$L_3 \dot{I}_3 + Q_3 \cdot \dot{z}_3 + R_3 I_3 = v_3$$
$$f_1 = K_1^1 I_1 + K_2^1 z_1 = K_1^1 I_1 + K_2^1 L\alpha$$
$$f_2 = K_1^2 I_2 + K_2^2 z_2 = K_1^2 I_2 + K_2^2 L \left(\sin \frac{\pi}{3} \cdot \beta - \sin \frac{\pi}{6} \cdot \alpha \right)$$
$$f_3 = K_1^3 I_3 + K_2^3 z_3 = K_1^3 I_3 + K_2^3 L \left(\sin \frac{\pi}{6} \cdot \alpha - \sin \frac{\pi}{3} \cdot \beta \right)$$
$$M\ddot{z} = f_1 + f_2 + f_3$$
$$J_{xx}\ddot{\alpha} = L \left(f_1 + f_2 \sin \frac{\pi}{6} + f_3 \sin \frac{\pi}{6} \right)$$
$$J_{yy}\ddot{\beta} = L \left(f_2 \sin \frac{\pi}{3} + f_3 \sin \frac{\pi}{3} \right).$$

Reorganizing, we get

$$\dot{I}_1 = -\frac{R_1}{L_1} I_1 - \frac{Q_1}{L_1}\dot{z} - \frac{Q_1 L}{L_1}\dot{\alpha} + \frac{1}{L_1} v_1$$

$$\dot{I}_2 = -\frac{R_2}{L_2} I_2 - \frac{Q_2}{L_2}\dot{z} + \frac{Q_2 L \sin \frac{\pi}{6}}{L_2}\dot{\alpha} - \frac{Q_2 L \sin \frac{\pi}{3}}{L_2}\dot{\beta} + \frac{1}{L_2} v_2$$

$$\dot{I}_3 = -\frac{R_3}{L_3} I_3 - \frac{Q_3}{L_3}\dot{z} - \frac{Q_3 L \sin \frac{\pi}{6}}{L_3}\dot{\alpha} + \frac{Q_3 L \sin \frac{\pi}{3}}{L_3}\dot{\beta} + \frac{1}{L_3} v_3$$

$$\ddot{z} = \frac{K_1^1}{M} I_1 + \frac{K_1^2}{M} I_2 + \frac{K_1^3}{M} I_3 + \frac{L(K_2^1 + \sin \frac{\pi}{6}(K_2^3 - K_2^2))}{M}\alpha$$
$$\quad + \frac{L \sin \frac{\pi}{3}(K_2^2 - K_2^3)}{M}\beta$$

$$\ddot{\alpha} = \frac{L K_1^1}{J_{xx}} I_1 - \frac{L K_1^2}{J_{xx}} I_2 - \frac{L K_1^3}{J_{xx}} I_3$$
$$\quad + \frac{L^2(K_2^1 + \sin^2 \frac{\pi}{6}(K_2^2 - K_2^3))}{J_{xx}}\alpha$$
$$\quad + \frac{L^2 \sin \frac{\pi}{6} \sin \frac{\pi}{3}(K_2^3 - K_2^2)}{J_{xx}}\beta$$

$$\ddot{\beta} = \frac{L K_1^2 \sin \frac{\pi}{3}}{J_{yy}} I_2 + \frac{L K_1^3 \sin \frac{\pi}{6}}{J_{yy}} I_3$$
$$\quad + \frac{L^2 \sin \frac{\pi}{6}(K_2^3 \sin \frac{\pi}{6} - K_2^2 \sin \frac{\pi}{3})}{J_{yy}}\alpha$$
$$\quad + \frac{L^2 \sin \frac{\pi}{3}(K_2^2 \sin \frac{\pi}{3} - K_2^3 \sin \frac{\pi}{6})}{J_{yy}}\beta.$$

Therefore, denoting the state, input, and output vector as

$$x = \begin{pmatrix} I_1 \\ I_2 \\ I_3 \\ z \\ \dot{z} \\ \alpha \\ \dot{\alpha} \\ \beta \\ \dot{\beta} \end{pmatrix}, \qquad u = \begin{pmatrix} v_1 \\ v_2 \\ v_3 \end{pmatrix}, \qquad y = \begin{pmatrix} K_3^1 z_1 \\ K_3^2 z_2 \\ K_3^3 z_3, \end{pmatrix} \qquad (11)$$

the state equations are

$$\dot{x} = Ax + Bu \qquad (12)$$
$$y = Cx \qquad (13)$$

which are the system matrices in (14), shown at the bottom of next page.

IV. DISCRETE DUAL-RATE CLOSED-LOOP MODELS AND CONTROL STRUCTURE

If the linear state equations (12) and (13) are discretized at a period T_0 (with zero-order hold at the input), we get

$$x((k+1)T_0) = Ax(kT_0) + Bu(kT_0) \qquad (15)$$
$$y(kT_0) = Cx(kT_0) + Du(kT_0). \qquad (16)$$

The state of each of the subsystems (to be used by each decentralized controller) will be denoted as x_i in the sequel, and the output as y_i. Obviously, the full state x above is composed by the juxtaposition of all x_i and, due to the inertial coupling, matrix A is not block-diagonal.
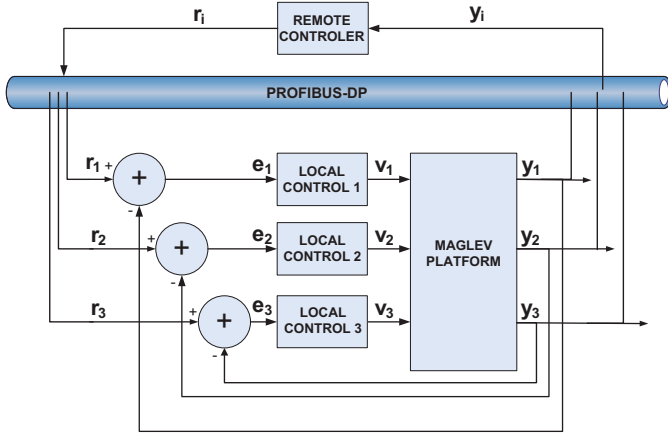
Fig. 5. Proposed hierarchical control system architecture, consisting of remote supervisory level controller, communications network, local controllers, and maglev platform.

Consider now the hierarchical control structure appearing in Fig. 5. This structure depicts multiple controllers controlling in a decentralized way the above plant, and a remote controller in charge of coordination.

Each subsystem has a one-degree-of-freedom local controller attached to it, whose state will be denoted as X_{Ci}, with equations given by

$$X_{Ci}((k+1)T_0) = A_d^{[i]} X_{Ci}(kT_0) + B_d^{[i]} e_i(kT_0) \quad (17)$$

$$v_i(KT_0) = C_d^{[i]} X_{Ci}(kT_0) + D_d^{[i]} e_i(kT_0) \quad (18)$$

where $e_i = r_i - y_i$ or, considering all of them in vector notation, $e = r - y$.

Obviously, the overall controller state equations of the local subsystem will have a block-diagonal structure: the notation X_C will denote the state of all controllers (juxtaposing each controller state in a larger vector). The state of the

controlled system (three-maglev platform) plus that of the local controllers will be denoted as $\chi = (x^T \ X_C^T)^T$. Obviously, although the controller state equations are block-diagonal, there will be some coupling due to the plant not being fully diagonal. The role of the remote controller will be to compensate such coupling neglected in the local decentralized side.

In order to achieve the coordination, the overall local subsystem equations will be considered in the form

$$\chi((k+1)T_0) = A_0 \chi(kT_0) + B_0 r(kT_0) \quad (19)$$

$$y(kT_0) = C_0 \chi(kT_0) + D_0 r(kT_0). \quad (20)$$

A. Dual-Rate Modeling

The remote system will be in charge of controlling the local subsystem over a network at a slower rate, because network limitations will be assumed to exist, limiting the sampling rate (see Section V).

The local controllers will be operating at a fast sampling rate with period T_0, and the remote controller at a slower rate $T = NT_0$. The network-induced round-trip time delay between a local controller sending y_i and receiving r_i will be denoted by $d_i(kT)$.

Some assumptions on the values of the delays in each loop are needed. Ample detail will be given in Section V, but at this moment we may preliminarily assert that, due to the chosen configuration of the Profibus communication, the sync and freeze commands will allow us to assume that the delay is coincident in all channels and multiple of the local sampling period. In the sequel, such delay will be denoted by $\delta(kT) = d(kT) \times T_0$. The value of $d(kT)$ will be assumed to be known at next sample time, given the sequence of network commands chosen for synchronization (see Section V for details).

$$A = \begin{pmatrix}
-\frac{R_1}{L_1} & 0 & 0 & 0 & -\frac{Q_1}{L_1} & 0 & -\frac{Q_1 L}{L_1} & 0 & 0 \\
0 & -\frac{R_2}{L_2} & 0 & 0 & 0 & -\frac{Q_2}{L_2} & \frac{Q_2 L \sin\frac{\pi}{6}}{L_2} & 0 & -\frac{Q_2 L \sin\frac{\pi}{3}}{L_2} \\
0 & 0 & -\frac{R_3}{L_3} & 0 & 0 & -\frac{Q_3}{L_3} & -\frac{Q_3 L \sin\frac{\pi}{6}}{L_3} & 0 & \frac{Q_3 L \sin\frac{\pi}{3}}{L_3} \\
0 & 0 & 0 & 0 & 1 & 0 & 0 & 0 & 0 \\
\frac{K_1^1}{M} & \frac{K_1^2}{M} & \frac{K_1^3}{M} & 0 & 0 & \frac{L(K_2^1+\sin\frac{\pi}{6}(K_2^3-K_2^2))}{M} & 0 & \frac{L\sin\frac{\pi}{3}(K_2^3-K_2^2)}{M} & 0 \\
0 & 0 & 0 & 0 & 0 & 0 & 1 & 0 & 0 \\
\frac{LK_1^1}{J_{xx}} & -\frac{LK_1^2}{J_{xx}} & -\frac{LK_1^3}{J_{xx}} & 0 & 0 & \frac{L^2(K_2^1+\sin^2\frac{\pi}{6}(K_2^2-K_2^3))}{J_{xx}} & 0 & \frac{L^2\sin\frac{\pi}{6}\sin\frac{\pi}{3}(K_2^2-K_2^3)}{J_{xx}} & 0 \\
0 & 0 & 0 & 0 & 0 & 0 & 0 & 0 & 1 \\
0 & \frac{LK_1^2\sin\frac{\pi}{3}}{J_{yy}} & \frac{LK_1^3\sin\frac{\pi}{6}}{J_{yy}} & 0 & 0 & \frac{L^2\sin\frac{\pi}{6}(K_2^3\sin\frac{\pi}{6}-K_2^2\sin\frac{\pi}{3})}{J_{yy}} & 0 & \frac{L^2\sin\frac{\pi}{3}(K_2^2\sin\frac{\pi}{3}-K_2^3\sin\frac{\pi}{6})}{J_{yy}} & 0
\end{pmatrix} \quad (14)$$

$$B = \begin{pmatrix}
\frac{1}{L_1} & 0 & 0 \\
0 & \frac{1}{L_2} & 0 \\
0 & 0 & \frac{1}{L_3} \\
0 & 0 & 0 \\
0 & 0 & 0 \\
0 & 0 & 0 \\
0 & 0 & 0 \\
0 & 0 & 0 \\
0 & 0 & 0
\end{pmatrix}, \quad C = \begin{pmatrix}
0 & 0 & 0 & K_3^1 & 0 & K_3^1 L & 0 & 0 & 0 \\
0 & 0 & 0 & K_3^2 & 0 & -K_3^2 L \sin\frac{\pi}{6} & 0 & K_3^2 L \sin\frac{\pi}{3} & 0 \\
0 & 0 & 0 & K_3^3 & 0 & K_3^3 L \sin\frac{\pi}{6} & 0 & -K_3^3 L \sin\frac{\pi}{3} & 0
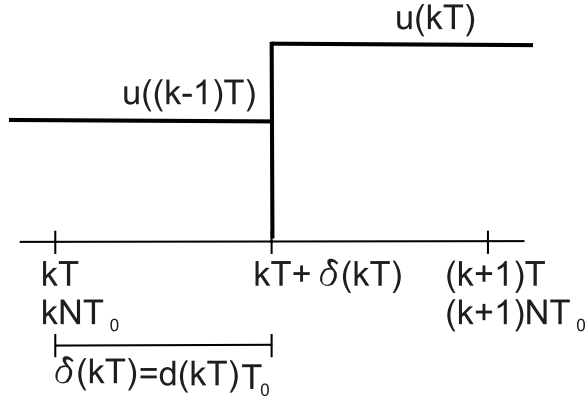\end{pmatrix}.$$

Fig. 6.   Control and state update chronogram.

Although the hierarchical control structure is reminiscent of a cascade control, conventional cascade-control design assumes a timescale separation so that a separate design is possible [25] and small delays would be negligible in the outer very low bandwidth loop. In the proposal here, the action of the remote controller will be fast enough to influence the stability and performance of the inner loop: bandwidth of both loops will be intentionally similar, and Lyapunov functions considering the whole remote+local+plant state will be needed.

1) Slow-Rate Modeling: In order to design the remote controller, a slow-rate model (at period $T = NT_0$) is needed.

Considering the fast-rate behavior (19), the slow-rate state update equations will be given by the well-known convolution expression [26]

$$\chi((k+1)NT_0) = A_0^N \chi(kNT_0)$$
$$+ \sum_{h=1}^{N} A_0^{h-1} B_0 r(((k+1)N - h)T_0). \quad (21)$$

However, as the reference input is updated after a delay of $\delta(kT) = d(kT)T_0$ and kept constant until next update (see Fig. 6), the above must be corrected to

$$\chi((k+1)NT_0) = A_0^N \chi(kNT_0) + \left(A_0^{N-d(kT)} \sum_{j=1}^{d(kT)} A_0^{j-1} B_0 \right)$$
$$\times r((k-1)NT_0) + \left(\sum_{i=1}^{N-d(kT)} A_0^{i-1} B_0 \right) r(kNT_0)$$
$$= A_0^N \chi(kNT_0) + B_1(N, d(kT))r((k-1)NT_0)$$
$$+ B_2(N, d(kT))r(kNT_0). \quad (22)$$

By assumption, T will be strictly greater than $d(kT)T_0 \ \forall k$, because the sampling period T has been selected in order to verify this restriction.[4] If $d(kT) > N$, the model would get

more complex, needing incorporation of further past values of r, i.e., $r((k-2)NT_0)$, etc. For simplicity, this issue will not be pursued further.

If an augmented state $\Psi(kT) = (\chi(kT), r((k-1)T)'$ referred to the remote period T is considered, the system as seen by the upper level can be expressed as

$$\Psi((k+1)T) = \begin{pmatrix} A_0^N & B_1(N, d(kT)) \\ 0 & 0 \end{pmatrix} \Psi(kT)$$
$$+ \begin{pmatrix} B_2(N, d(kT)) \\ I \end{pmatrix} r(kT). \quad (23)$$

For brevity in further developments, notations A^* and B^* are introduced in (23), yielding

$$\Psi((k+1)T) = A^*(N, d(kT))\Psi(kT)$$
$$+ B^*(N, d(kT))r(kT). \quad (24)$$

The modeling procedure in Section III allows obtaining the above matrices in the experimental platform.

B. Control Design Strategy

Having described the dual-rate modeling and notation, this section discusses general ideas on the chosen control design methodologies.

Basically, on one hand, three low-order (and hence with low computational requirements) local controllers will be designed using standard mixed-sensitivity $\mathcal{H}_\infty$ control techniques [15], assuming a decoupled system.

On the other hand, LMI gridding and the nonstationary Kalman filter are used in the coordinating remote controller (in [16] and [27] for the basic formulae for the LMI-gridding approach, and in [28] and [29] for the Kalman filter), assuming a fully coupled plant.

In this section, the control techniques in the remote side are reviewed for convenience. Note, importantly, that in order to develop this control system structure, the delay $d(kT)$ must be known. Conditions for applicability of a separation principle are also discussed in [16].

1) LMI Gridding: From the augmented model (24), the control synthesis problem can be cast as a state-feedback one, leading to

$$r(kT) = -F^* \Psi(kT). \quad (25)$$

However, the gain F^* must ensure robustness against the unknown round-trip delay $d(kT)$ because its value is not known *a priori* at the time when $r(kT)$ is computed, its value will be later obtained by using the freeze/sync commands, but it will be useful only for the *a posteriori* observer part.

In order to achieve stabilizing controllers subject to time-varying delays, an LMI gridding procedure [16] is considered. From [16], there exist matrices X and M so that (26), shown

---

$$\begin{bmatrix} e^{-2\vartheta T} X & X(A^*(N, d(kT)))^T - M^T(B^*(N, d(kT)))^T \\ A^*(N, d(kT))X - B^*(N, d(kT))M & X \end{bmatrix} > 0 \qquad (26)$$

---

[4]For this purpose, some experimental offline tests have been done to determine the maximum round-trip delay.
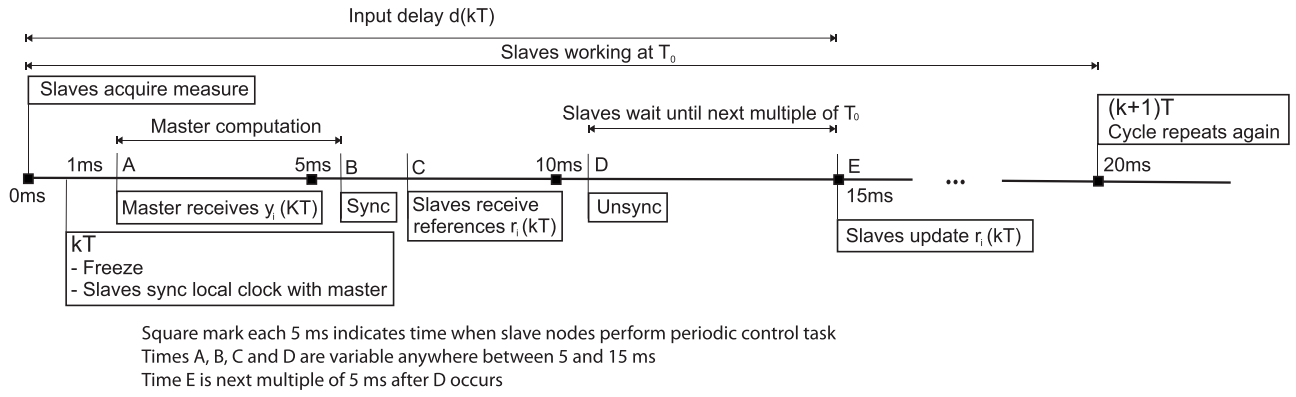
Fig. 7. Coordination and synchronization chronogram (Profibus implementation of Figs. 5 and 6).

on the bottom of previous page is verified for any $d(kT)$ which may arise in experimental operation: in this particular application, $d(kT)$ takes values in $[1, \ldots, N-1]$.

If the LMIs are feasible, the feedback controller $F^* = MX^{-1}$ stabilizes (24) with decay rate ϑ (continuous-time equivalent), and $\Psi(kT)^{\mathrm{T}} X^{-1} \Psi(kT)$ is the associated Lyapunov function. As discussed in Section V, the experimental setup required $N = 4$ and gridding on possible values of $d(kT) = 1, 2, 3$, so (26) is actually a collection of three LMIs.

2) Nonstationary Kalman Filter: Regarding the observer design for (24), as $d(kT)$ can be obtained from freeze/sync commands at the time when $r((k+1)T)$ is computed, Kalman gains depending on induced delays can be obtained with nonstationary Kalman filters [30], [31], whose equations are as follows:

$$P(kT) = A^*(N, d(kT))\Lambda(kT)A^*(N, d(kT))^T + V(kT)$$
$$(27)$$

$$L(kT) = P(kT)C^T(CP(kT)C^T + W(kT))^{-1} \qquad (28)$$

$$\Lambda((k+1)T) = (I - L(kT)C)P(kT) \qquad (29)$$

where $V(kT)$ and $W(kT)$ are process and measurement noise parameters. The observer gain is $L(kT)$, with an estimated state, denoted by $\tilde{\Psi}(kT)$, obtained via the current-observer update equation

$$\tilde{\Psi}(kT) = (I - L(kT)C)$$
$$\times \left(A^*(N, d((k-1)T)\tilde{\Psi}((k-1)T) \right.$$
$$\left. + B^*(N, d((k-1)T)r(kT) \right) + L(kT)y(kT).$$
$$(30)$$

In order to implement the above equation, the packet received by the remote node should contain the array of measurements $y(kT)$, the time in which they were measured, and the delay $d((k-1)T)$ in the preceding cycle as explained in the next section.

V. HARDWARE AND NETWORK CONFIGURATION

The control experiments developed in this paper have been implemented as follows.

In the first level, the local controllers have been implemented using a National Instruments CompactRIO device as shown in Fig. 2 (right).

The network was a Profibus-DP; its nodes were a ComSoft DFProfi-II DP card in the PC and a Profibus module cRio PB in the compactRio controller, the latter operating as a bus master. Details on the network elements can be found in http://www.comsoft.de and http://www.ni.com.

The available Profibus-DP bandwidth enables us to use a second level where a remote coordinating control action is injected at just every 20 ms. Indeed, the chosen Profibus configuration parameter was a bus rate of 187.5 kbits/s with asynchronous operation.

Let us now discuss how the remote control and local-level synchronization are carried out. Every $T = 20$ ms, the supervisor controller starts the control task as follows (symbolicaly depicted in Fig. 7).

1) *Stage 1:* Master node sends freeze command to slave nodes. All slaves receive the message at approximately the same time (with some microseconds jitter due to the bus cycle) and freeze the inputs (from the process). In the next Profibus cycle, slaves send frozen inputs (measures) to master node. Receiving freeze command is used also for synchronizing slave clocks to $t = 1$ ms.

2) *Stage 2:* Master node receives the measures from slaves and process data according to the control algorithm.

3) *Stage 3:* Master node sends sync command to slave nodes. Then, their outputs to the process are internally updated at the next Profibus cycle in the buffers but not applied until an unsync command is received.

4) *Stage 4:* Master node sends the referred unsync command to slaves, and then all of them update the outputs (reference to local controllers) simultaneously at the next multiple of the local sampling time T_0. As the remote controller knows the moment in which it sent the unsync command, it can compute $d(kT)$ for the observer update.

5) *Stage 5:* With their internal sampling time $T_0 = 5$ ms, local controllers perform the platform control algorithm with no communication with the master node. At sampling time $T = 20$ ms, the measurements are taken and stored in the buffer. The master node starts again the control process at $t = 21$ ms, and the sequence returns to stage 1.

Delay	5 ms	10 ms	15 ms
Occurrences	123 154	1 084 502	292 357
Percentage	8.21%	72.3%	19.49%

A. Distribution of Round-Trip Delays d(kT)

An experimental test was conducted to measure the magnitude of the network-induced time delays: the most repeated round-trip time delay corresponds to a 10-ms period, with eventual delays at 5 and 15 ms, as shown in Table I. For this reason, the grid of times for discretizing the system will be formed by the set of values (5, 10, 15) ms.

VI. NUMERICAL RESULTS AND EXPERIMENTS

In this section, the numerical results of the controller computations and the experimental measurements will be described.

Note that, although it is theoretically possible to control a linear system with a discrete-time controller at any desired period, the disturbance rejection and tolerance to modeling errors severely diminish as such period increases with unstable systems. This fact is proved to be fundamental in our experiments, in the following sense.

1) The $\mathcal{H}_\infty$ controllers designed for the long period $T = 20$ ms were, in actual experiments, not able to stabilize even a single maglev in a local configuration with no network delay, even though they were of course stable in the simulations. Hence, the slow-rate remote-only control option was not a viable solution.

2) On the other hand, a local controller at each of the levitators with a SISO loop may be a viable solution. Indeed, local stabilizing controllers at $T_0 = 5$ ms with the decoupled model were obtained by $\mathcal{H}_\infty$ techniques, and were able to stabilize appropriately a single maglev.

3) However, due to disregarded couplings, modeling error is introduced which will degrade performance of the local-only decentralized controllers, as later experiments show. Of course, incorporating the coupling would require communication between the different subsystems, assumed to be feasible only via the chosen network (at a slower rate).

In summary, the above issues justify the need for the proposed dual-rate structure.

In order to deal with these issues, a set of experiments have been developed, as follows.

A. Preliminary Experiments: Single-Maglev Control

First of all, a preliminary experiment with a single maglev, not with the whole platform, has been developed. In this experiment, first, a standalone $\mathcal{H}_\infty$ controller has been designed and implemented. This type of controller is chosen in the local controller in order to suitably balance disturbance rejection performance versus tolerance to modeling errors at particular frequencies.
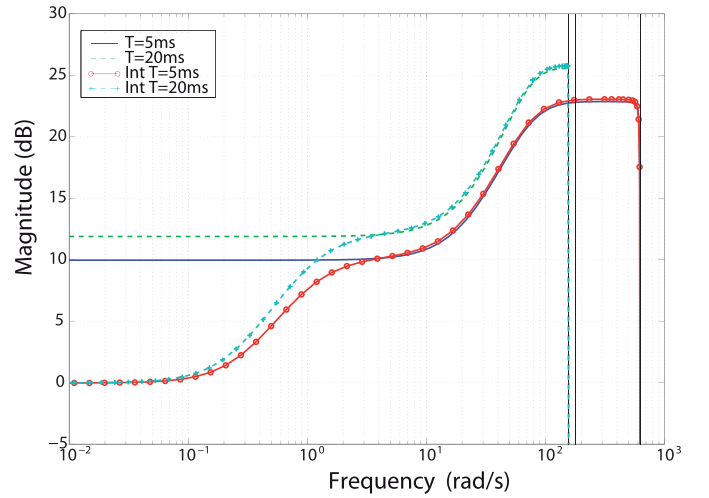

Fig. 8.   System's sensitivity to additive uncertainty with different sampling rates.

A first set of controllers are designed for each single maglev using a mixed-sensitivity approach using a set of weight values, i.e., sensitivity weight, control action weight, and complementary sensitivity weight. For the designed controllers, the values of these corresponding weights are 1, 0.2, and 0.6. Using the robust toolbox MATLAB command [K, CL, GAM, INFO] = MIXSYN(G, 1, 0.2, 0.6), where G is the equivalent discrete model plant for state space maglev model, the different local controllers for each of the three maglevs are obtained. Weights have been chosen as constants to keep the resulting controller order low.

Experimentally, a set of controllers has been designed using several sampling periods keeping the same design parameters. As a result of all the experiments, the greatest sampling period that could be satisfactorily used with the maglev was $T_0 = 5$ ms: with larger sampling periods, accumulated error can become too large, so it makes the one-maglev system unstable or on the verge of instability.

Fig. 8 shows the additive uncertainty sensitivity analysis, i.e., $K/(1 + KG)$, when controller and plant (for a single maglev) are sampled at 5 and 20 ms. As the sampling time increases, uncertainty in model and sensitivity increases, making the experimental system unstable.

As all the local controllers are very similar, the numerical value of just one of them is

$$G_R(z) = \frac{u(z)}{e(z)} = \frac{10.845(z+1)(z-0.878)(z-0.641)}{(z+0.93)((z-0.54)^2 + 0.27^2)}. \tag{31}$$

An additional set of controllers is designed by adding an (approximate) integral term. Defining the continuous integrator as $(G(\tau s + 1)/G\tau s + 1)$, with a large enough G and a small enough τ, this continuous term is discretized at T_0 sampling time using Tustin discretization method. This discretized term is included in the sensitivity weight (W_I) for calculating the new controller. In our case, the resulting weight was $(W_I(z) = (1.001z - 0.9982)/(z - 0.9997))$. A new controller is designed using this integrator term in the sensitivity weight (WI) [K, CL, GAM, INFO] = MIXSYN(G, WI, 0.2, 0.6). As a

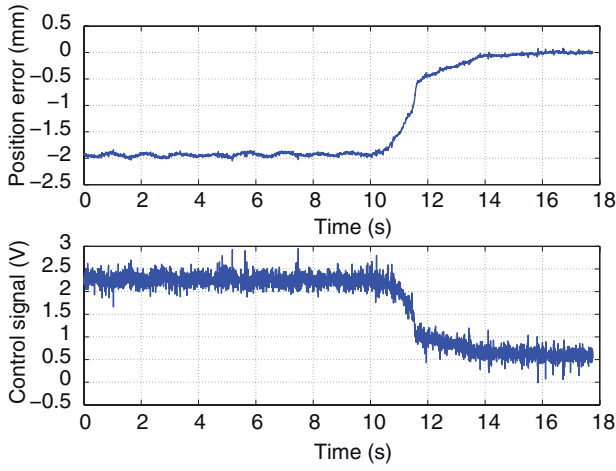Fig. 9. Single maglev experiment.

Fig. 10. Platform position in Experiments 1 and 2.

result, the new set of controllers is obtained. One of them is

$$G_R(z) = \frac{10.74(z+1)(z-0.99)(z-0.88)(z-0.71)}{(z-1)(z+0.94)((z-0.56)^2+0.28^2)} \quad (32)$$

which, as expected, is very similar to (31) except at low frequencies.

With these numerical results, a first preliminary single-maglev experiment is developed, whose output appears in Fig. 9. The experiment begins by activating the local controller without the integrator [see (31)]. The system achieves an equilibrium point with position error, as expected, but the system performance is suitable. At time $t = 10.5$ s, the controller changes adding the integral term [see (32)] and, after a 2-s transient, the system achieves the new equilibrium point with no position error. This experiment is performed with only one standalone maglev. After this experiment is concluded, the platform is assembled with the tree maglevs, and the rest of experiments below are carried out.

In summary, this preliminary experiment demonstrates that the chosen design parameters for the local controllers allow an adequate SISO control performance for the real plant.

B. Experiment 1: Three-Maglev Platform, No Network

This experiment is developed using the whole platform and the set of local controllers previously developed without integral action (31). Therefore, the network and the supervisor level are not used yet. The experiment starts with platform at the equilibrium point and, at time $t = 2.5$ s, a load change is applied to the platform depositing a 2-euro coin in the center of the triangular aluminum structure. As seen in Fig. 10, the system response seems to change to a new equilibrium point (i.e., position error) but it barely keeps there, and the platform becomes unstable and drops at $t = 5.5$ s.

This is the result of coupling between the different maglevs in the whole platform system as single-maglev controllers worked perfectly when isolated.
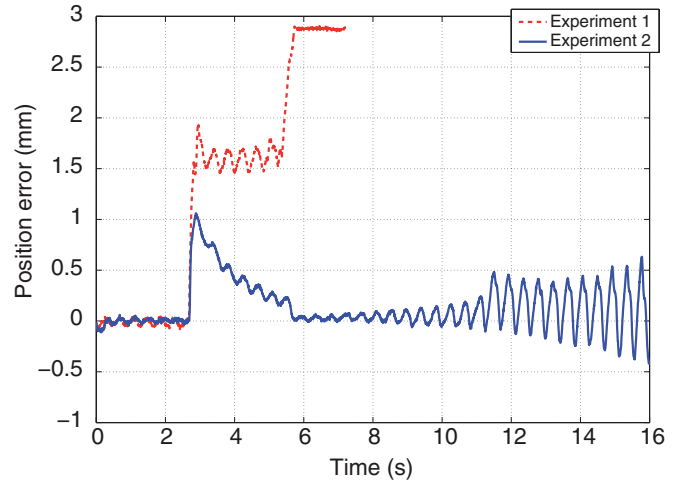
C. Experiment 2: Three-Maglev Platform, No Network, Integral Action

This experiment is the same as the previous one but using controllers with the integral action included, as in (32). As in the previous experiment, network and supervisor level are not used yet.

Although the integrator tries to recover the reference position, oscillations of increasing amplitude are generated due to the load disturbance and, ultimately, the loop becomes unstable and the platform falls.

With these two experiments (Experiments 1 and 2), the coupling in platform is demonstrated to be significant, and it must be taken into account when designing the control system.

D. Experiment 3: Three-Maglev Platform, Hierarchical Control, No Integrator

This third experiment is developed using the network and an additional supervisor-level controller. Each maglev on the platform keeps its own local controller (no integral action) as previously designed, i.e., the same set of controllers used as in Experiment 1, see (31).

At the higher level, in the remote side, a plant model is developed following the results in previous sections, where the considered process is the set composed by the three maglev systems and the corresponding local digital control subsystems with period T_0.

The resulting state feedback controller (25) obtained has a gain matrix of dimensions 3×21 as shown in Section (VI-E) depicted top on page 10.

This supervisor controller is implemented on remote side, jointly with the previously discussed observer.

The experiment starts with platform at the equilibrium point, as shown in Fig. 11. At time $t = 1.75$ s, a load is applied, and after a transient, the system acquires a new stable equilibrium point, but with position error (as expected). Compared to Experiment 1, now the supervisor control level compensates for the disturbances introduced by the coupling between the three maglevs of the platform.
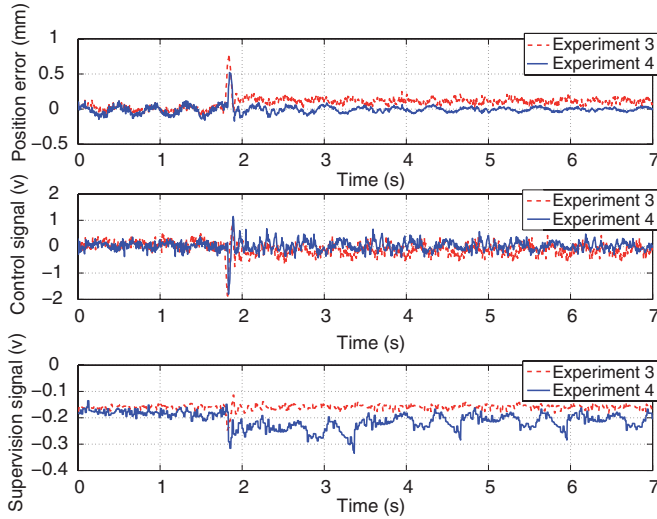
Fig. 11. Results for Experiments 3 and 4.

	Maglev 1	Maglev 2	Maglev 3
Resistance [Ω]	$R_1 = 4.6$	$R_2 = 5$	$R_3 = 4.2$
Inductance [mH]	$L_1 = 52$	$L_2 = 73$	$L_3 = 32$
Em. transfer gain [N/A]	$K_1^1 = -0.56$	$K_1^2 = -0.7$	$K_1^3 = -0.82$
Position transfer gain [N/m]	$K_2^1 = 98$	$K_2^2 = 98$	$K_2^3 = 98$
Sensor transfer gain [V/m]	$K_3^1 = 680$	$K_3^2 = 700$	$K_3^3 = 705$

The new controller with the integral action can keep the platform stable even with load variations. The integral component works at a low rate because it is present in the supervisor level, on the remote side of the controller. As Fig. 11 shows, after the load is applied to the platform, the system keeps the stable equilibrium point obtaining acceptable results in terms of performance.

VII. CONCLUSION

In this paper, a practical Profibus-DP network-based control application has been developed in order to coordinate an unstable triangular maglev platform via a dual-rate controller implementation.

Both local-only and network-only controllers were unable to satisfactorily stabilize the platform. However, a hierarchical control structure succeeded in the experiments. A simple stabilization local control and a refined LMI-based + Kalman filter solution in the remote side allowed us to solve the problem caused by the limited network bandwidth and time-varying delays.

Even though a particular choice of controller/observer strategy has been experimentally demonstrated, for more demanding applications (out of the scope of this paper), the results might be ameliorated by including further theoretical developments, such as delay uncertainty (slight desyncrhonization), or delay-dependent Lyapunov functions, even incorporating information on the probabilistic distribution of the delays.

APPENDIX

A. Magnetic Levitation Model Parameters

As previously mentioned, some of the maglev parameters have been identified by manufacturer and are listed in the maglev user's manual. Those parameters, for the three maglevs here used, are shown in Table II.

As a result of the experimental identification, the values $Q^1 = Q^2 = Q^3 = 0.5$ Vs/m have been assigned. The length of the structure arm L is 0.117 m (see Fig. 4), and the total weight of platform, including load, M is 0.406 kg. The

In Fig. 11, the top figure shows the position error (center of mass), the middle one shows the control signal applied to maglev, and the bottom one shows the supervision signal generated by the supervisor controller and sent through the network to the local controller. For clarity, only one of the three control and supervision signals is plotted.

E. Experiment 4: Three-Maglev Platform, Hierarchical Control, Integrator (Remote)

The results obtained with Experiment 3 present position error; so for obtaining a stable plant without position error, a new remote controller that includes accumulated error in state system is developed. So the controller is designed considering

$$\begin{pmatrix} \Psi((k+1)T) \\ s((k+1)T) \end{pmatrix} = \begin{pmatrix} A^* & 0 \\ -C^* & I \end{pmatrix} \begin{pmatrix} \Psi(kT) \\ s(kT) \end{pmatrix} + \begin{pmatrix} B^* \\ -0 \end{pmatrix} r(kT) \tag{34}$$

where the position error in $C^*\Psi$ will be zero in the steady state [29].

Following this reasoning, the system state vector is expanded adding the accumulated error for each one of the three maglevs on the levitated platform. According to this new plant model, the feedback state controller is recalculated obtaining a new state feedback gain, also with LMI gridding.

As the system model vector state has been increased with the new states corresponding to the accumulated errors, the new feedback gain increases their dimensions, which in this case is a matrix of size 3×24.

$$F^* = \begin{pmatrix} -5.36 & 383.2 & -0.63 & 44.76 & -0.001 & -0.008 & 0.57 & 0.001 & 0 & 0.22 & 0.12 & -0.013 \\ -4.75 & 349.4 & 0.29 & -20.32 & -0.5 & 35.34 & -0.003 & 0.33 & -0.0003 & -0.003 & -0.120 & 0 \\ 1.963 & 395.7 & -0.11 & -23.14 & -0.19 & 40.08 & 0.0004 & -00002 & 0.06 & 0.0008 & 0.037 & -0.0001 \end{pmatrix}$$

$$\begin{matrix} \dots & 0.001 & 0.044 & 0 & 0.001 & 0.012 & 0 & 0.104 & 0.0004 & 0 \\ \dots & 0.194 & -2.45 & -0.008 & -0.001 & -0.02 & 0 & -0.001 & 0.06 & -0.001 \\ \dots & 0.0001 & 0.007 & 0 & 0.042 & -6.86 & -0.004 & 0.001 & 0 & -0.15 \end{matrix} \tag{33}$$

inertia matrix

$$\begin{pmatrix} J_{xx} & J_{xy} & J_{xz} \\ J_{yx} & J_{yy} & J_{yz} \\ J_{zx} & J_{zy} & J_{zz} \end{pmatrix} = \begin{pmatrix} 0.00293 & 0 & 0 \\ 0 & 0.00293 & 0 \\ 0 & 0 & 0.00541 \end{pmatrix}$$

has been obtained via CAD software (modeling the object with solid geometry, assigning the weights and obtaining inertial data from the CAD analysis module).

Noise matrices used in Kalman filter, V and W, are diagonal matrices with values of 0.0062 and 0.01, respectively. Measurement noise W is deduced by obtaining sensor measures with the still platform, mechanically fixed. The variations measured about mean value correspond to noise and this value is used for characterizing the matrix. V characterizes input noises and modeling errors, and it has been adjusted experimentally to obtain suitable observer dynamics.

REFERENCES

[1] Y. Tipsuwan and M. Chow, "Control methodologies in networked control systems," *Control Eng. Pract.*, vol. 11, no. 10, pp. 1099–1111, 2003.

[2] Y. Halevi and A. Ray, "Integrated communication and control systems. I-Analysis," *ASME, Trans. J. Dynamic Syst., Meas. Control*, vol. 110, pp. 367–373, Dec. 1988.

[3] T. Yang, "Networked control system: A brief survey," *IEE Proc.-Control Theory Appl.*, vol. 153, no. 4, pp. 403–412, Jul. 2006.

[4] S. Banerjee, D. Prasad, and J. Pal, "Design, implementation, and testing of a single axis levitation system for the suspension of a platform," *ISA Trans.*, vol. 46, no. 2, pp. 239–246, Apr. 2007.

[5] W. Kim, S. Verma, and H. Shakir, "Design and precision construction of novel magnetic-levitation-based multi-axis nanoscale positioning systems," *Precis. Eng.*, vol. 31, no. 4, pp. 337–350, 2007.

[6] W. Kim, K. Ji, and A. Ambike, "Real-time operating environment for networked control systems," *IEEE Trans. Autom. Sci. Eng.*, vol. 3, no. 3, pp. 287–296, Jul. 2006.

[7] J. Paddison, H. Ohsaki, and E. Masada, "Control strategies for Maglev electromagnetic suspension bogies," in *Proc. 35th IEEE Decision Control*, vol. 3. Dec. 1996, pp. 2796–2797.

[8] R.-J. Wai and J.-D. Lee, "Performance comparisons of model-free control strategies for hybrid magnetic levitation system," *IEE Proc.-Electr. Power Appl.*, vol. 152, no. 6, pp. 1556–1564, Nov. 2005.

[9] P. Holmer, "Faster than a speeding bullet train," *IEEE Spectrum*, vol. 40, no. 8, pp. 30–34, Aug. 2003.

[10] P. Berkelman and M. Dzadovsky, "Large motion range magnet levitation using a planar array of coils," in *Proc. IEEE Int. Conf. Robot. Autom.*, May 2009, pp. 3950–3951.

[11] D. Hristu-Varsakelis and W. S. Levine, *Handbook of Networked and Embedded Control Systems*. Boston, MA: Birkhäuser, 2008.

[12] K. Lee, S. Lee, and M. Lee, "Remote fuzzy logic control of networked control system via Profibus-DP," *IEEE Trans. Ind. Electron.*, vol. 50, no. 4, pp. 784–792, Aug. 2003.

[13] Z. Lie-Ping, Z. Yun-Sheng, and Z. Qun-Ying, "Remote control based on OPC and Profibus-DP bus," *Control Eng. China*, vol. 5, pp. 594–597, May 2008.

[14] V. Casanova, J. Salt, A. Cuenca, and V. Mascarós, "Networked control systems over Profibus-DP: Simulation model," in *Proc. IEEE Int. Conf. Control Appl.*, Oct. 2006, pp. 1337–1342.

[15] K. Zhou, *Essentials of Robust Control*. Englewood Cliffs, NJ: Prentice-Hall, 1998.

[16] A. Sala, "Computer control under time-varying sampling period: An LMI gridding approach," *Automatica*, vol. 41, no. 12, pp. 2077–2082, Dec. 2005.

[17] C. Fernández, M. Vicente, and L. Jiménez, "Virtual laboratories for control education: A combined methodology," *Int. J. Eng.*, vol. 21, no. 6, pp. 1059–1067, 2005.

[18] R. Fama, R. Lopes, A. Milhan, R. Galvão, and B. Lastra, "Predictive control of a magnetic levitation system with explicit treatment of operational constraints," in *Proc. 18th Int. Congr. Mech. Eng.*, Ouro Preto, MG, 2005, pp. 1–8.

[19] K. Erkan and T. Koseki, "Fuzzy model-based monlinear Maglev control for active vibration control systems," *Int. J. Appl. Electromagn. Mech.*, vol. 25, no. 1, pp. 543–548, 2007.

[20] H. Han-Hui and T. Qing, "Decoupling fuzzy PID control for magnetic suspended table," *J. Central South Univ. Sci. Technol.*, vol. 4, pp. 963–968, Apr. 2009.

[21] N. Al-Muthairi and M. Zribi, "Sliding mode control of a magnetic levitation system," *Math. Probl. Eng.*, vol. 2, no. 2004, pp. 93–107, 2004.

[22] J. E. Marsden and J. Scheurle, "The reduced Euler-Lagrange equations," in *Proc. Fields Instrum. Commun.*, 1992, pp. 139–164.

[23] J. Van Bladel, *Electromagnetics Fields*. New York: Wiley, 1964.

[24] A. El Hajjaji and M. Ouladsine, "Modeling and nonlinear control of magnetic levitation systems," *IEEE Trans. Ind. Electron.*, vol. 48, no. 4, pp. 831–838, Aug. 2001.

[25] K. Ogata, *Modern Control Engineering*. Englewood Cliffs, NJ: Prentice-Hall, 2010.

[26] P. Albertos, "Block multirate input-output model for sampled-data control systems," *IEEE Trans. Autom. Control*, vol. 35, no. 9, pp. 1085–1088, Sep. 1990.

[27] A. Sala, "Improving performance under sampling-rate variations via generalized hold functions," *IEEE Trans. Control Syst. Technol.*, vol. 15, no. 4, pp. 794–797, Jul. 2007.

[28] R. F. Stengel, *Optimal Control and Estimation*. New York: Dover, 1994.

[29] A. Sala, *Multivariable Control Systems: An Engineering Approach*. New York: Springer-Verlag, 2004.

[30] J. Tornero, R. Pizá, P. Albertos, and J. Salt, "Multirate LQG controller applied to self-location and path-tracking in mobile robots," in *Proc. IEEE/RSJ Int. Conf. Intell. Robots Syst.*, vol. 2. Aug. 2001, pp. 625–630.

[31] M. Mora, R. Pizá, and J. Tornero, "Multirate obstacle tracking and path planning for intelligent vehicles," in *Proc. IEEE Intell. Veh. Symp.*, Jun. 2007, pp. 172–177.

Ricardo Pizá received the B.Eng. and Ph.D. degrees in control engineering from Valencia Technical University, Valencia, Spain, in 1997 and 2003, respectively.

He is currently an Assistant Professor with the Universitat Politècnica de València, Valencia. He has authored or co-authored several papers in journals and conferences, and has been involved in several research projects funded by local industries and government. His current research interests include network-based control systems, computer-aided manufacturing, and robotics.

Julián Salt (M'07) received the M.Sc. degree in industrial engineering and the Ph.D. degree in control engineering from the Technical University of Valencia, Valencia, Spain, in 1986 and 1992, respectively.

He is a Full Professor with the Technical University of Valencia, where he is currently the Head of the Department of Systems Engineering and Control. He has been a supervisor of nine Ph.D. theses. He has co-authored over 70 papers in journals and conferences. His current research interests include nonconventionally sampled control and networked control systems.

Antonio Sala (M'03) was born in Valencia, Spain, in 1968. He received the B.Eng. degree (Hons.) in combined engineering from Coventry University, Coventry, U.K., in 1990, and the M.Sc. degree in electrical engineering and the Ph.D. degree in control engineering from Valencia Technical University, Valencia, in 1993 and 1998, respectively.

He has been with the Universitat Politecnica de Valencia, Valencia, since 1993, where he is currently a Full Professor and the Vice-Head of the Systems and Control Engineering Department. He has supervised five Ph.D. theses and more than 25 final M.Sc. projects. He has been involved in several research and mobility projects funded by local industries, government, and European community. He has authored or co-authored more than 40 journal papers (25 works with more than 10 cites, H-index is 18).

Dr. Sala has been member of the IFAC Publications Committee for eight years. He is an Associate Editor of the IEEE TRANSACTIONS ON FUZZY SYSTEMS.
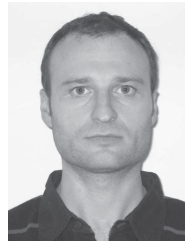
Ángel Cuenca (M'06) received the M.Eng. degree in computer engineering and the Ph.D. degree in control engineering from the Technical University of Valencia, Valencia, Spain, in 1998 and 2004, respectively.

He has been with the Department of Systems Engineering and Control, Technical University of Valencia, since 2000, where he is currently an Associate Professor. He has been involved in several research projects funded by Spanish government, and European community. He has authored or co-authored over 40 journal and conference papers. His current research interests include multirate control systems, networked control systems, and event-based control systems.